

ULRIKE HOMBERG, DANIEL BAUM, ALEXANDER
WIEBEL, STEFFEN PROHASKA, HANS-CHRISTIAN HEGE

Definition, Extraction, and Validation of Pore Structures in Porous Materials

Herausgegeben vom
Konrad-Zuse-Zentrum für Informationstechnik Berlin
Takustraße 7
D-14195 Berlin-Dahlem

Telefon: 030-84185-0
Telefax: 030-84185-125

e-mail: bibliothek@zib.de
URL: <http://www.zib.de>

ZIB-Report (Print) ISSN 1438-0064
ZIB-Report (Internet) ISSN 2192-7782

Definition, Extraction, and Validation of Pore Structures in Porous Media

U. Homberg, D. Baum, A. Wiebel, S. Prohaska, H.-C. Hege

September 19, 2013

Abstract

An intuitive and sparse representation of the void space of porous materials supports the efficient analysis and visualization of interesting qualitative and quantitative parameters of such materials. We introduce definitions of the elements of this void space, here called pore space, based on its distance function, and present methods to extract these elements using the extremal structures of the distance function. The presented methods are implemented by an image processing pipeline that determines pore centers, pore paths and pore constrictions. These pore space elements build a graph that represents the topology of the pore space in a compact way. The representations we derive from μ CT image data of realistic soil specimens enable the computation of many statistical parameters and, thus, provide a basis for further visual analysis and application-specific developments. We introduced parts of our pipeline in previous work. In this chapter, we present additional details and compare our results with the analytic computation of the pore space elements for a sphere packing in order to show the correctness of our graph computation.

1 Introduction

Soil materials of different particle size distributions form pore structures exhibiting different properties that impact the transport processes of particles through the pore space. Kinds of internal erosion like suffusion comprise such transport processes and may weaken the particle structure of the soil and, thus, its stability. To investigate the risk of suffusion, it is important to know which parts of the pore space can be reached by particles of what size. The size as well as the portions of such mobile particles provide information on the stability of the soil.

For the assessment of soil properties, an understanding of the three-dimensional formations and arrangements of its particles and its pore structure may be of great benefit. To gain insight into soil structures, CT scans of realistic and undisturbed soil material can be acquired and analyzed.

An analysis of the pore space and possible transport pathways needs information on pore space elements like pores, constrictions, and paths. While the pores and their connecting paths determine where particles can move, the constrictions define the size of the particles that can move from one pore to another. Thus, a complete representation that preserves the arrangement and the connectivity of these pore space elements enables an efficient analysis of transport paths, blocking constrictions and sizes of potentially mobile particles.

We previously described [10] the pore space elements based on the extremal structures of the distance map of the pore space and presented methods to extract

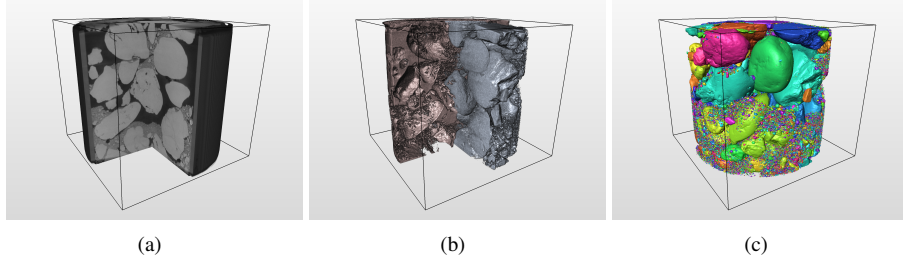


Figure 1: CT scan of soil material: (a) volumetric image data, (b) particles and pore space, (c) separated particles colored according to their identifier.

these structures. The proposed methods start from a segmentation of the soil structure [11] and generate a graph that is a geometric embedding into the pore space and compactly represents the topology of the pore space. This approach avoids anabranches that are caused by irregular particles. A hierarchical merge process enables a clustering of pores by the significance of their connecting constrictions.

In this chapter, we present a validation of the extracted pore structures. For this purpose, we first recall parts of our approach with additional details and then present a comparison with the result of an exact Voronoi graph algorithm applied to a sphere packing to measure the quality of our results.

2 Related Work

Existing methods analyze the pore space at different levels of detail. Statistical approaches use simple methods for phase segmentation and to compute parameters and distributions on the pore-solid relations [3, 9, 16, 20]. In these methods, measurements of the captured pore space as a whole are proposed, but a localization and differentiation of pores is not considered.

Other approaches differentiate the pore space elements and investigate the networks they build. One possibility is to use the maximal inscribed spheres map, which is equal to the distance map [12] of the pore space. Sweeney et al. [23] and Silin et al. [22] accomplish the differentiation of pores and constrictions by evaluating and classifying the neighboring spheres. Both works compute a stick-and-ball diagram representing the pore bodies and their connectivity. However, computing the pore volumes based on spheres leads to an underestimation of the pore size.

Skeleton-based methods [6, 14, 15] determine the medial axes of the pore space and use morphological tools to classify the skeleton voxels as belonging to a path or a constriction. Their representations enable the construction of a geometrically embedded graph and the determination of parameters like numbers and sizes of constrictions. These approaches, however, need removal processes to avoid surface-like structures or anabranches caused by isolated particles or irregular particle surfaces.

Some approaches make use of concepts from Morse theory. For example, Ushizima et al. [25] use Reeb graphs to analyze the permeability and maximum flow of gas through porous networks. In contrast to the method we describe, their method depends on the orientation of the data set, that is, on height information in the data set. Gyulassy et al. [8] compute and simplify the Morse-Smale complex of the distance map to extract filament structures in porous solids, which results in

a medial axes-related representation. The result depends on the degree of simplification and may produce a superset of the structures we aim to extract.

Another way to analyze pores and constrictions is based on Delaunay/Voronoi partitions. While Reboul [19] uses Delaunay tetrahedrons and their faces to specify the pore bodies and constrictions for sphere packings, Lindow et al. [13] compute the paths from the Voronoi cells of a sphere packing. Glantz [7] proposes an extension to irregular shaped particles in voxel data, where the corners of the pore space boundary are tessellated. This results in time-consuming computations and produces many anabranches. Thompson [24] generates a Delaunay tessellation of the particle centers obtained from distance extrema within the particle regions. However, this is not applicable to the realistic soil material of our samples, because the particles have irregular shapes and, thus, multiple distance extrema.

Some authors address the problem of fragmented pores and propose pairwise merge criteria that are based on overlapping spheres [1, 19, 22, 24] or on relations of radii and distances of pores [15]. Such relations allow one to cluster fragmented pores, but elongated pores may stay separated. Also, these pairwise considerations may cluster pores even if there is a significant constriction in the middle. This is, for example, the case when several neighboring pores gradually increase and decrease in size with minor constrictions in between.

3 Determination of the Pore Structure

The methods we present here have been developed to process CT scans of specimens produced from soil aggregates. These scans are acquired at a resolution of $39 \mu\text{m}$ [2]. Figure 1(a) shows a volumetric visualization of the dual soil structures of such a CT scan, that is, the particles and pore structure (Figure 1(b)). To assess the complex pore space, we follow the intuition of particle transport, where a pathway locally runs with maximal distance to the surrounding soil structure and the bottlenecks determine the maximal size of particles that can move along the path. We start with the three-dimensional image domain $I \subset \mathbb{R}^3$, which can be separated into foreground (particle structure) $F \subset I$ and background (pore space) $B = I \setminus F$. For the computation of the pore space elements, we need a particle segmentation (Figure 1(c)) where all particles are well separated and each particle has its own identifier [11].

3.1 Defining the Elements of the Pore Structure

Most of the approaches in the literature use methods that encode the distance relations within the pore space. We follow this idea and describe the features of the pore space by the three-dimensional signed distance map [12] $d : I \rightarrow \mathbb{R}$ according to the boundaries between the segmented foreground F and background B , where each image point is assigned the distance as follows:

$$d(p) = \begin{cases} \min_{q \in F} \|p - q\|, & \text{if } p \in B \\ -\min_{q \in B} \|p - q\|, & \text{if } p \in F \end{cases} \quad (1)$$

To describe the pore structures, we use the extremal structures of the distance map (Figure 2). These are the critical points c where the gradient of the distance function vanishes, that is $\nabla d(c) = 0$, as well as the integral lines γ of the gradient that allow a grouping into stable and unstable manifolds [4]. The critical points of a 3D function are the maxima c_{max} , the minima c_{min} , and the two types of saddle points (index-1 c_{S1} , index-2 c_{S2}). The integral lines are defined as $\gamma : \mathbb{R} \rightarrow \mathbb{R}^3$ whose tangential vectors are parallel to the gradients of d , $\dot{\gamma} = \nabla d(\gamma(t))$ for

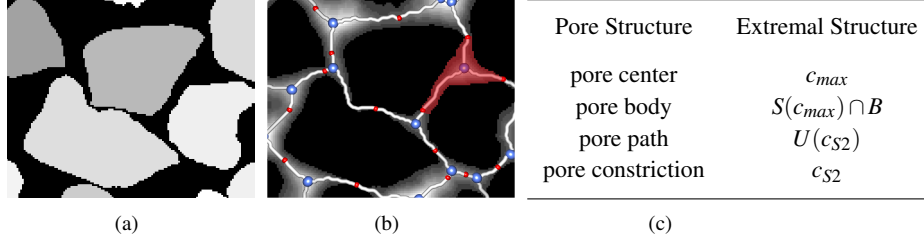


Figure 2: Illustration of the pore space elements (b) between particles (a): Pore centers (blue), paths (white), constrictions (red), pore bodies (red region). The figures are two-dimensional for clarity of the illustration. (c) Link between pore structures and extremal structures of the distance map.

each $t \in \mathbb{R}$, and connect two critical points where $orig(\gamma) = \lim_{t \rightarrow -\infty} \gamma(t)$ is called the origin and $dest(\gamma) = \lim_{t \rightarrow \infty} \gamma(t)$ the destination. Each regular point r , where $\nabla d(r) \neq 0$, is part of an image of γ and can be assigned to the critical points that are connected by γ . These assignments describe the manifolds, where the direction or opposite direction distinguishes between stable or unstable manifolds:

$$\text{stable manifolds:} \quad S(c) = \{c\} \cup \{r \in d \mid r \in \text{im}\gamma, \text{dest}(\gamma) = c\} \quad (2)$$

$$\text{unstable manifolds:} \quad U(c) = \{c\} \cup \{r \in d \mid r \in \text{im}\gamma, \text{orig}(\gamma) = c\} \quad (3)$$

Because the distance values of d are positive within the pore space B , the maxima c_{max} mark those points where the distance is maximal to the surrounding particles. We define these points to be the pore centers. The index-2-saddle points c_{S2} of the 3d distance map and their unstable manifolds $U(c_{S2})$ connect two maxima. They depict the paths from one pore center to another along the maximal distance to the surrounding particles. An index-2-saddle point is the point along a path between two connected maxima having the smallest distance and it corresponds, in terms of pore structure elements, to the pore constriction, which determines the maximal size of particles that can move from one pore to another. Finally, a pore body consists of all points in the pore space B that end in the same maximum when following the steepest ascent. The table in Figure 2(c) summarizes these correspondences.

3.2 Voxel-based Determination of the Pore Space Skeleton

The defined pore space elements, that is, pore centers, paths, and constrictions, form a network representing the pore space topology. We previously proposed the following voxel-based processing pipeline to extract these elements [10]. Starting point is the segmentation result, where the foreground F covers the whole particle structure and decomposes it into separated particles F_i , which are labeled by their identifier i .

In the processing pipeline illustrated in Figure 3, we use the correspondence between our distance-based definitions and a Voronoi decomposition. In case of a set of points, a Voronoi cell of a Voronoi point consists of all points whose distance is not greater than their distance to any other Voronoi point. The distances on the facets, edges, and vertices of the Voronoi cells are maximal to the closest two, three, or four Voronoi points, respectively. Looking at the distance function according to the Voronoi points, the Voronoi vertices are located at the maxima, and the Voronoi edges are located at the index-2-saddles and their unstable manifolds.

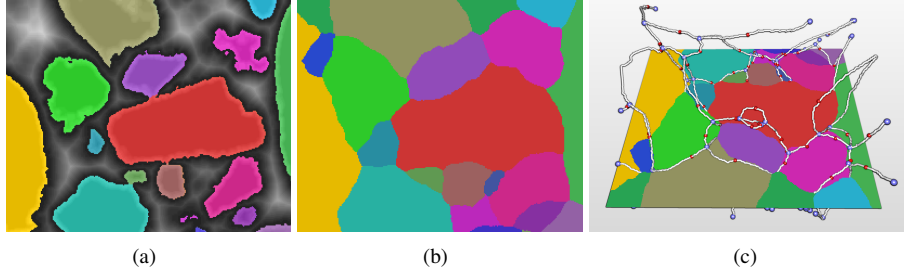


Figure 3: Pore graph computation: (a) slice of labeled particles and distance information, (b) propagated particle regions, (c) pore graph constructed from the boundaries of the propagated regions. The colors of the graph elements correspond to Figure 2.

The processing pipeline detects these locations between the particles according to the boundary voxels of the segmented particles instead of according to single Voronoi points.

Decomposition. The three-dimensional signed distance map with regard to the boundaries between foreground and background is computed according to equation 1. Distance values within the foreground F are negative while distances within the background B are positive. The labeled particles are used as seeds for a watershed transformation [21] that propagates the particles according to increasing distance. As a result, each voxel of the pore space is assigned the identifier of its nearest particle, such that the image volume I is completely partitioned into the propagated particle regions V_i , which meet at points having equal distances to the particles:

$$V_i = \{F_i\} \cup \left\{ p \in B \mid \min_{q \in F_i} \|p - q\| \leq \min_{s \in F_j} \|p - s\|, \forall j \neq i \right\} \quad (4)$$

Skeleton. Next, the boundaries of the particle regions are evaluated in order to determine the pore space skeleton. We identify voxel neighborhoods of size $2 \times 2 \times 2$ that contain labels of three or more particle regions V_i , because these are the neighborhoods that contain points having equal distance to at least three particles. For each such neighborhood, we mark a representative voxel (the bottom, left, front voxel) in the resulting volume. All other voxels of the result are marked as background. With this approach, we remove paths that are only surrounded by two or less particles. These paths can occur in case of neighboring concave particles and build isolated and/or small anabranches. Particles that can move there do not change the soil structure and its stability. Therefore, these paths are negligible.

Pore graph. The identified skeleton may have segments with a thickness of more than one voxel. In order to remove these, we apply thinning [18]. Finally, we construct a graph structure by converting this skeleton into vertices, edges and edge points [17]. The resulting graph represents the pore centers by its vertices and the paths by its edges. The edges additionally have edge points and contain radius information at each point. This allows one to mark the point with the smallest radius on each edge as constriction and provides information about the spatial course of the paths and the distances.

3.3 Merging Unstable Pores

Due to the irregular shape and arrangement of particles, multiple local maxima resp. pore centers may appear, as denoted in Figure 4. The yellow, orange, and

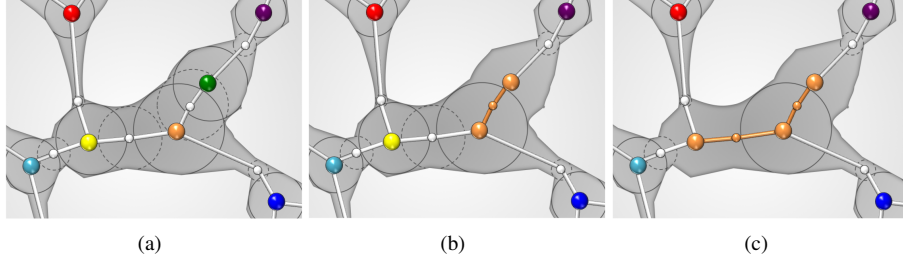


Figure 4: Hierarchical merge of (a) pores (colored vertices and black circles) separated by their constrictions (white points and dotted circles): (b) the green and orange pores merge; the green pore and the common constriction are assigned the orange representative; the constriction between green and purple is now between the orange representative and the purple one. (c) Merge of the non-overlapping yellow and orange pores.

green pore centers seem to belong to a single pore. This may lead to an under- or overestimation of parameters like pore size and constriction number. Therefore, we merge such pore centers in the following post-processing step.

The method is inspired by topological persistence and simplification [5]. Topological persistence assesses the features of a function by their significance. We use the radius differences of a constriction and their connected pore centers as persistence measure. If the difference is high, the pores are significantly separated by their connecting pore constriction and stay separated. In turn, pore centers that are connected by a constriction having almost the same radius as the pore centers will be merged. The degree of the merge depends on a user-defined threshold.

The algorithm hierarchically merges and updates neighboring pairs of pore centers and their radius differences (Algorithm 1). Each edge, its adjacent vertices and a difference value will be represented by an edge tuple, where the difference value is given by the minimum radius difference of the two vertices to the constriction on this edge. The pore center having the larger radius is set to be the representative vertex of the edge tuple. When an edge and a vertex are merged to their representative, the incident edges of the merged vertex will be updated: The edges and the representatives of their vertices build new edge tuples.

Finally, adjacent vertices having the same representative and their connecting edges will be labeled as belonging to the same pore. As a result, merged pore centers, paths and constrictions can be specifically included or excluded from the quantification tasks. The maximal diameter of a pore is then given by the distance information of the representative vertex of the merged pore.

4 Comparison

The voxel-based pipeline described in Section 3 enables us to analyze the pore space of realistic data containing particles of irregular shape. However, the voxel-based methods suffer from inaccuracies due to the discrete nature of the data. The inaccuracies may even accumulate during processing a pipeline of voxel-based methods. Because we generally apply our pipeline to realistic data, there is no possibility to measure the quality of our pipeline on these data sets, because we do not have any ground truth for the realistic data.

As mentioned above, our pipeline generates a decomposition of the voxel data set such that each voxel is assigned to its nearest segmented particle. This de-

Algorithm 1 Hierarchical Merge

```
1: input: Graph  $G(V, E)$ , threshold  $t$ 
2: UnionFindSet  $UFS \leftarrow \{v_n : v_n \in V, n = 1, \dots, N\}$   $\triangleright$  With radius as rank
3: Heap  $H \leftarrow \{ (v_1, v_2, e, diff) : v_1, v_2 \in V, e \in E, \text{radius}(v_1) < \text{radius}(v_2),$ 
4:    $diff = \text{radius}(v_1) - \text{radius}(e) \}$   $\triangleright$  Edge tuples sorted by  $diff$ 
5:  $currTuple \leftarrow H.\text{extractMin}()$ 
6: while  $currTuple.diff < t$  do
7:    $UFS.\text{union}(currTuple.v_1, currTuple.v_2)$ 
8:   for all  $incTuple \leftarrow \text{incidentTo}(currTuple.v_1, G)$  and  $incTuple \neq currTuple$  do
9:      $v_1 \leftarrow UFS.\text{find}(incTuple.v_1)$ 
10:     $v_2 \leftarrow UFS.\text{find}(incTuple.v_2)$ 
11:     $e \leftarrow incTuple.e$ 
12:    if  $\text{radius}(v_1) > \text{radius}(v_2)$  then  $\text{swap}(v_1, v_2)$ 
13:     $newDiff \leftarrow (\text{radius}(v_1) - \text{radius}(e))$ 
14:     $newTuple \leftarrow (v_1, v_2, e, newDiff)$ 
15:     $H.\text{remove}(incTuple)$ 
16:     $H.\text{insert}(newTuple)$ 
17:   end for
18:   if  $H.\text{empty}()$  then break
19:    $currTuple \leftarrow H.\text{extractMin}()$ 
20: end while
21:  $\text{relabel}(G, UFS)$   $\triangleright$  Labels vertices & connecting edges according to the  $UFS$  components
```

composition is related to a Voronoi decomposition. Hence, we call the extraction pipeline Voronoi-like pore space computation.

In order to evaluate the results of our method, we have therefore chosen a sphere packing as comparison basis for two reasons. First, sphere packings are commonly used to simulate porous materials in the area of geotechnics. Second, for sphere packings, it is possible to compute an analytic description of the topology of the distance transform of the spheres by applying an algorithm that computes the Voronoi diagram of spheres (see, for example, Lindow et al. [13]). By considering the result of the analytic algorithm as ground truth, we are able to evaluate the results of our voxel-based Voronoi-like pore graph computation.

4.1 Comparison Data

The input to the analytic Voronoi diagram algorithm is a set of weighted points given by the sphere centers of the sphere packing, where the weights are the radii of the spheres. The output of the algorithm is an analytic description of the edge graph of the Voronoi diagram (Fig. 5(c)). This is given by the Voronoi vertices, that is, the vertices, where four Voronoi regions meet, and the Voronoi edges between these vertices. To compare the Voronoi graph with the pore graph resulting from the voxel-based pore space computation, we sample the edges of the Voronoi graph, such that neighboring points on the edges have a maximum distance smaller than a given threshold D_s . For each of these sample points, which we call edge points, as well as for the Voronoi vertices, we also store the minimal distance to any of the neighboring spheres. This distance corresponds to the radius of the maximal ball located at these points without intersecting the spheres.

To compute the pore graph of the sphere packing, we first have to compute a voxel representation of the sphere packing (Fig. 5(b)). The result is a labeled voxel data set, where each voxel is assigned the label of the sphere it belongs or 0 if it belongs to the pore space. The pipeline then computes the pore graph (Fig. 5(d)) of the sphere packing, consisting of the pore centers, which correspond to the

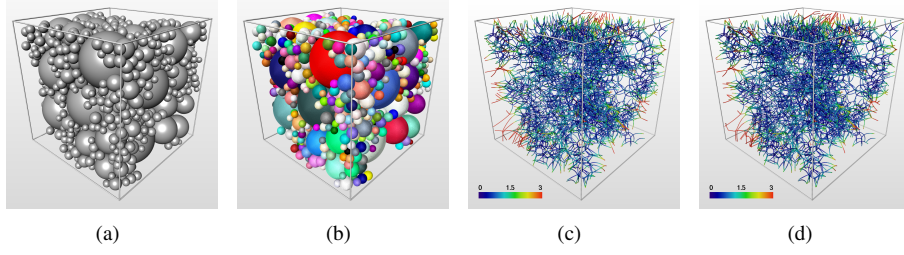


Figure 5: Comparison data: sphere packing (a) and voxelized spheres (b), Voronoi graph (c) and pore graph (d) with radius information.

Voronoi vertices, and the pore paths, which correspond to the Voronoi edges. We did not sample the pore paths, because they already have edge points on them with a distance corresponding to the voxel size.

4.2 Graph Matching

Now we have two graphs $G_1 = (V_1, E_1, P_1)$ and $G_2 = (V_2, E_2, P_2)$ representing the Voronoi graph and the pore graph, respectively. Here, V_1 and V_2 are the sets of vertices corresponding to the local maxima of the distance transformation, both in the analytical and the discrete case. E_1 and E_2 are the sets of edges, which are not directly considered in the comparison but only via the sets P_1 and P_2 , which represent the edge points. We further define the radius functions $d_i : V_i \cup P_i \rightarrow \mathbb{R}$ that assign to each vertex or edge point the minimal distance to any of the neighboring particles or spheres.

To measure the difference of G_1 to G_2 , we are interested in two things. (I) How much differ the two graphs geometrically? The geometric distance can be calculated by determining the shortest distance of each vertex in V_1 to any vertex in V_2 . Similarly, we need to determine the shortest distance of each point in P_1 to any point in P_2 . (II) How much differs the radius information on the graphs? The radius gives the size of the constrictions, which are of particular interest to us. For this, we need matchings $m_{V12} : V_1 \rightarrow V_2$ with $m_{V12}(v) = \operatorname{argmin}_w \|v - w\|$ and $m_{P12} : P_1 \rightarrow P_2$ with $m_{P12}(p) = \operatorname{argmin}_q \|p - q\|$, where $v \in V_1, w \in V_2, p \in P_1, q \in P_2$ and $\|\cdot\|$ denotes the Euclidean length. Note that the matchings m_{V12} and m_{P12} are, in general, not bijections. This is not a problem, because the matchings are only a means to compute the geometric differences between the graphs. Given the matchings, we can then compute the differences between the radius information of the matched vertices and edge points as $|d_i(v) - d_i(m_{12}(v))|$ and $|d_i(p) - d_i(m_{12}(p))|$, respectively, where $|\cdot|$ denotes the absolute value. We use an octree to efficiently compute m_{V12} and m_{P12} .

5 Results and Discussion

In this section, we compare our voxel-based pipeline to the Voronoi graph computation on the basis of a sphere packing. We will not discuss results of the pipeline applied to realistic data. Such results are available in our previous work [10].

The comparison was carried out using a sphere packing of 1250 spheres of varying radii (1.5 to 5.2mm), which were placed in a box of 50mm×50mm×50mm. For the voxel-based pipeline, we scan-converted the sphere packing into a voxel data set. We chose a sampling rate of 50 voxels per minimal sphere diameter. This resulted in a voxel size of 40μm×40μm×40μm corresponding to the resolution

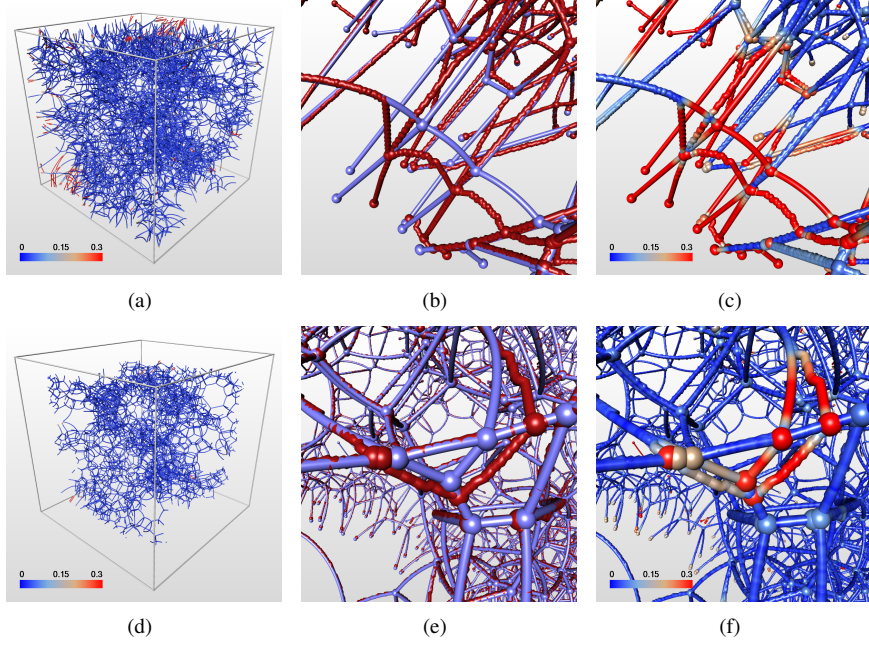


Figure 6: Differences between pore graph and Voronoi graph. (a) Color-coded distances between the matched points and vertices. (b) Close-up of the bottom left corner in (a): pore graph (red) and Voronoi graph (blue). (c) Distances color-coded on the same close-up. (d) The graphs are trimmed by 5mm from each side. (e) and (f) Close-ups with many pore centers and Voronoi vertices.

of our CT scans. The resulting data set had a size of $1250 \times 1250 \times 1250$ voxels. The computation of the Voronoi graph took less than two seconds while the voxel-based pipeline took 52 minutes. The edges of the Voronoi graph were sampled with a maximal distance $D_s = 0.05mm$.

We applied the matching procedure described in Section 4. Figure 6 depicts images showing the vertex and edge point distances between the two graphs. If we consider the complete graphs (Figure 6(a)), we can observe that the main differences lie at the border in regions where there is a large empty space (also see Figure 5(a)). The reason for this large empty space is that no spheres were placed in this region due to restrictions caused by the border. As a result, we get long pore paths ending at the border (see, for example, the left bottom corner in Figure 6(a) which has been zoomed in in Figures 6(b) and (c)). The further away the pore path is from the nearest spheres, the smaller is the difference in the distances when looking orthogonally around the pore path. Hence, small differences in the distances to the nearest spheres correspond to large differences in the position of the pore path. Thus, small errors in the computation of the distances can result in large errors of the pore path position. For the statistics we want to carry out later, trimming the graph gives us much more realistic data. The graphs in Figure 6(d) were trimmed by 5mm from each side. The major differences that remain between the graphs after trimming appear in regions where many pore centers/Voronoi vertices occur (see, for example, the close-ups in Figures 6(e) and (f)). Here, small errors in the distances to the nearest spheres might result in either pores being merged or split. Hence, too many pore centers or Voronoi vertices, respectively, as well as pore paths or Voronoi edges occur, which results in the observed differences. The

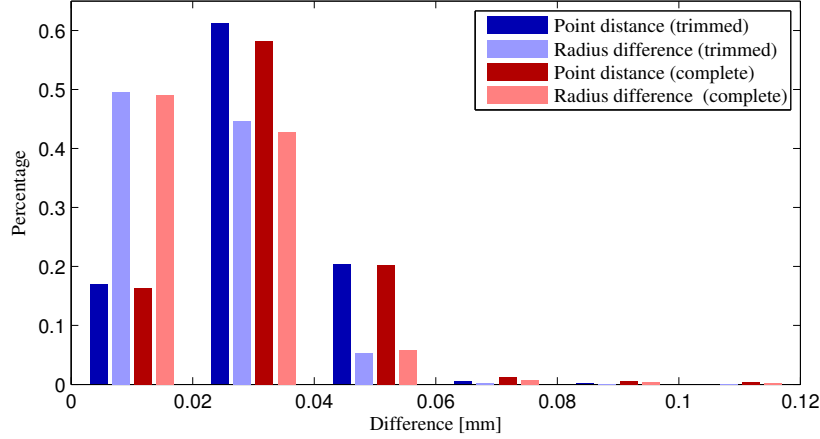


Figure 7: Differences between matched edge points of the pore graph and the Voronoi graph. Only the bins summing up to 99 percent of each of the distribution are plotted.

distances between the pore centers and the Voronoi vertices are largest, because they can only get matched to one another.

Figure 7 shows the histogram of the comparison measures for the complete pore graph in red and the pore graph with trimmed boundary region in blue. The distances are plotted in dark and the radius differences in light red and light blue. As mentioned above, we trimmed the pore graph by $5mm$ from each side to eliminate boundary effects. This is important for the final analysis of the pore space, because the constrictions on edges near the boundaries exhibit unrealistic radius values due to the restricted growth of the distance map towards the boundary. This, in turn, would lead to biased statistics on the pore constrictions.

It is obvious that the accuracy of the voxel-based computation depends on the resolution of the data set. Taking into account the voxel size, we binned the data points with a bin size of $0.02mm$. This corresponds to half the voxel length. Regarding the distances between the edge points (dark colored bars), this means, that the matched edge points of the first group can be assumed to lie within the same voxel and the points of the second and third group within the direct neighborhood. Furthermore, we assume the radius differences (bright colored bars) within the three first groups to lie on the same or on the very next distance iso-value, whether they share the same position or not.

Accumulating the first three bins shows that 94.9 percent of the edge points of the untrimmed and 98.6 percent of the trimmed graph match the edge points of the Voronoi graph at least within the direct neighborhood. According to this, the edge points of the first three bins exhibit a radius difference to the Voronoi edge points of less than $0.06mm$. This concerns 97.8 percent of the edge points of the untrimmed graph and 99.5 percent of the trimmed graph. It is worth noting that regarding the aim of analyzing the transport pathways for particles of certain sizes, the radius information along a path is even more important than the exact position of points along the path way. The maximal error is $0.79mm$ and $0.34mm$ in point distance and radius difference of the trimmed pore graph. Such discrepancies mainly occur at the boundary (Figure 6(c)) and only make up a very small fraction of the whole set of edge points. Above all, the presented matching procedure is only able to provide an upper bound of the error. Because it matches each edge point from one graph to the other even if there is no direct correspondence, large differences in

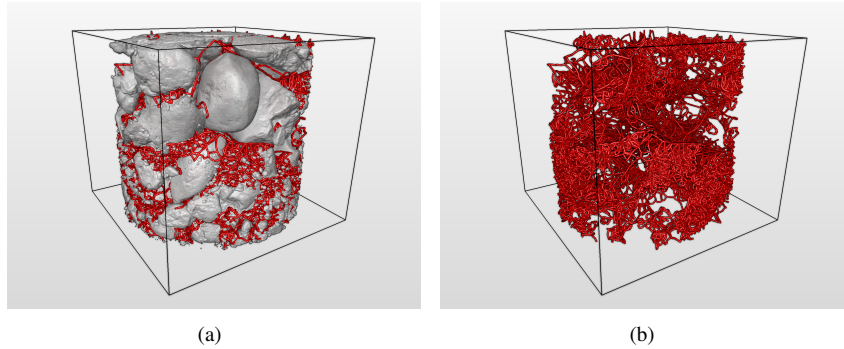


Figure 8: Pore graph (a) with and (b) without the particle structure computed from a CT scan of soil.

the distance and the radius comparison measure may be acquired in these cases. In Figure 7 we can see that the error of 99 percent of our edge points is below $0.12mm$ which is less than a tenth of the radius of the smallest sphere in the packing. We can assume that the errors of the remaining one percent of edge points do not invalidate conclusions that can be drawn from derived statistics of the extracted pore structures.

6 Conclusion

We have described a method to extract the topology of the pore space in a porous material and validated the results of our method based on an analytic example. Regarding the given details, the presented description of the method goes beyond what is available in our previous work. Thus, it allows for a straight forward implementation of the pipeline. Comparing our pore graph to the Voronoi graph of the analytic sphere packing example allowed us to analyze the accuracy and validity of our approach. The analysis has shown that differences between the graphs are mostly in the scale of one voxel and, thus, the accuracy is very high. Together with a simultaneous visual inspection of the two graphs, the high accuracy allowed us to illustrate the validity of our approach. Since the computation of the pore space elements for a sphere packing does not differ from that for a realistic data set, we conclude that our method works also correct for realistic data.

Acknowledgement

This work was partly funded by the German Research Foundation (DFG) in the project “Conditions of suffusive erosion phenomena in soil”. Special thanks go to Norbert Lindow for providing his implementation of the Voronoi graph algorithm.

References

- [1] R. Al-Raoush, K. Thompson, and C. S. Willson. Comparison of network generation techniques for unconsolidated porous media. *Soil Science Society of America Journal*, 67(6):1687–1700, 2003.
- [2] R. Binner, U. Homberg, S. Prohaska, U. Kalbe, and K. J. Witt. Identification of descriptive parameters of the soil pore structure using experiments and ct

- data. In *Proceedings of the 5th International Conference Scour and Erosion (ICSE-5)*, pages 397–407, 2010.
- [3] M. E. Coles, R. D. Hazlett, P. Spanne, W. E. Soll, E. L. Muegge, and K. W. Jones. Pore level imaging of fluid transport using synchrotron X-ray micro-tomography. *Journal of Petroleum Science and Engineering*, 19(1-2):55–63, 1998.
 - [4] H. Edelsbrunner, J. Harer, and A. Zomorodian. Hierarchical morse complexes for piecewise linear 2-manifolds. In *Proceedings of the 17th Annual Symposium on Computational Geometry*, pages 70–79. ACM, 2001.
 - [5] H. Edelsbrunner, D. Letscher, and A. Zomorodian. Topological persistence and simplification. *Discrete and Computational Geometry*, 28(4):511–533, 2002.
 - [6] R. Glantz. *Porennetzwerke von Erdstoff-Filtern mathematisch-morphologische Beschreibung kernspintomographischer Aufnahmen*. PhD thesis, University Karlsruhe, Karlsruhe, 1997.
 - [7] R. Glantz and M. Hilpert. Dual models of pore spaces. *Advances in Water Resources*, 30(2):227–248, 2007.
 - [8] A. Gyulassy, M. Duchaineau, V. Natarajan, V. Pascucci, E. Branga, A. Higinbotham, and B. Hamann. Topologically clean distance fields. *IEEE Transactions on Visualization and Computer Graphics*, 13(6):1432–1439, 2007.
 - [9] M. Hadwiger, L. Fritz, C. Rezk-Salama, T. Höllt, G. Geier, and T. Pabel. Interactive volume exploration for feature detection and quantification in industrial ct data. *IEEE Transactions on Visualization and Computer Graphics*, 14(6):1507–1514, 2008.
 - [10] U. Homberg, D. Baum, S. Prohaska, U. Kalbe, and K. J. Witt. Automatic extraction and analysis of realistic pore structures from μ ct data for pore space characterization of graded soil. In *Proceedings of the 6th International Conference Scour and Erosion (ICSE-6)*, pages 66–73, 2012.
 - [11] U. Homberg, R. Binner, S. Prohaska, V. J. Derksen, A. Kuß, and U. Kalbe. Determining geometric grain structure from x-ray micro-tomograms of graded soil. In K. J. Witt, editor, *Internal Erosion*, volume 21 of *Schriftenreihe Geotechnik*, pages 37–52, 2009.
 - [12] M. W. Jones, J. A. Bærentzen, and M. Sramek. 3d distance fields: A survey of techniques and applications. *IEEE Transactions on Visualization and Computer Graphics*, 12(4):581–599, 2006.
 - [13] N. Lindow, D. Baum, and H.-C. Hege. Voronoi-based extraction and visualization of molecular paths. *IEEE Transactions on Visualization and Computer Graphics*, 17(12):2025–2034, 2011.
 - [14] W. B. Lindquist, S.-M. Lee, D. A. Coker, K. W. Jones, and P. Spanne. Medial axis analysis of void structure in three-dimensional tomographic images of porous media. *Journal of Geophysical Research*, 101(B4):8297–8310, 1996.
 - [15] W. B. Lindquist, A. Venkatarangan, J. Dunsmuir, and T. Wong. Pore and throat size distributions measured from synchrotron X-ray tomographic images of fontainebleau sandstones. *Journal of Geophysical Research*, 105(B9):21509–21527, 2000.
 - [16] A. Pierret, Y. Capowiez, L. Belzunces, and C. J. Moran. 3d reconstruction and quantification of macropores using X-ray computed tomography and image analysis. *Geoderma*, 106(3-4):247–271, 2002.
 - [17] S. Prohaska. *Skeleton-Based Visualization of Massive Voxel Objects with Network-Like Architecture*. PhD thesis, University of Potsdam, 2007.

- [18] C. Pudney. Distance-ordered homotopic thinning: A skeletonization algorithm for 3d digital images. *Computer Vision and Image Understanding*, 72(3):404–413, 1998.
- [19] N. Reboul, E. Vincens, and B. Cambou. A statistical analysis of void size distribution in a simulated narrowly graded packing of spheres. *Granular Matter*, 10(6):457–468, 2008.
- [20] F. Rezanezhad, W. L. Quinton, J. S. Price, D. Elrick, T. R. Elliot, and R. J. Heck. Examining the effect of pore size distribution and shape on flow through unsaturated peat using 3-d computed tomography. *Hydrology and Earth System Sciences*, 13(10):1993–2002, 2009.
- [21] J. B. T. M. Roerdink and A. Meijster. The watershed transform: Definitions, algorithms and parallelization strategies. *Fundamenta Informaticae*, 41(1–2):187–228, 2001.
- [22] D. Silin and T. Patzek. Pore space morphology analysis using maximal inscribed spheres. *Physica A: Statistical and Theoretical Physics*, 371(2):336–360, 2006.
- [23] S. M. Sweeney and C. L. Martin. Pore size distributions calculated from 3-D images of DEM-simulated powder compacts. *Acta Materialia*, 51(12):3635–3649, 2003.
- [24] K. E. Thompson, C. S. Willson, C. D. White, S. Nyman, J. P. Bhattacharya, and A. H. Reed. Application of a new grain-based reconstruction algorithm to microtomography images for quantitative characterization and flow modeling. *SPE Journal*, 13(2):164–176, 2008.
- [25] D. M. Ushizima, D. Morozov, G. H. Weber, A. G. C. Bianchi, and E. W. Bethel. Augmented topological descriptors of pore networks for material science. *IEEE Transactions on Visualization and Computer Graphics*, 18(12):2041–2050, 2012.